Unravelling the switching mechanisms in electric field induced insulator–metal transitions in VO$_2$ nanobeams

Servin Rathi[1], Jin-Hyung Park[1], In-yeal Lee[1], Jeong Min Baik[2], Kyung Soo Yi[3] and Gil-Ho Kim[1]

[1] School of Electronic and Electrical Engineering and Sungkyunkwan Advanced Institute of Nanotechnology (SAINT), Sungkyunkwan University, Suwon 440-746, Korea
[2] School of Mechanical and Advanced Materials Engineering, Ulsan National Institute of Science and Technology (UNIST), Ulsan 689-805, Korea
[3] Department of Physics, Pusan National University, Busan 609-735, Korea

E-mail: ghkim@skku.edu

Abstract
We studied insulator–metal transitions in VO$_2$ nanobeams for both abrupt and gradual changes in applied electric fields. Based on the observations, the Poole–Frenkel effect explained the abrupt transition, while the gradual case is found to be dominated by the Joule heating phenomenon. We also carried out power model and finite element method based simulations which supported the Joule heating phenomena for gradual transition. An in-principle demonstration of the Poole–Frenkel effect, performed using a square voltage pulse of 1 μs duration, further confirms the proposed insulator–metal transition mechanism with a switching time in the order of 100 ns. Finally, conductivity variations introduced via rapid thermal annealing at various temperatures validate the roles of both Joule heating and Poole–Frenkel mechanisms in the transitions.

Keywords: vanadium dioxide nanobeams, Joule heating, Poole–Frenkel effect, insulator–metal transitions

(Some figures may appear in colour only in the online journal)

1. Introduction

Despite having half-filled 3d shells, electron localization resulting from strong electron–electron interactions makes vanadium dioxide (VO$_2$) an insulator at room temperature [1]. However, this behaviour can be overcome by the application of external stimuli like heat, dopants, electric fields, strain and light, which leads to a transition from an insulating to a metallic state [2, 3]. Below the transition temperature (T_C), the atomic arrangement in VO$_2$ is monoclinic (M1), and the pairing and tilting of V^{4+} ions results in the localization of the outer 3d electrons. Coulombic repulsion at the localization sites opens up an energy gap of 0.6 eV via the splitting of the d orbitals, which produces a highly resistive insulating state. However, for temperatures above T_C, dissociation and reorientation of

the vanadium pairs into periodic chains parallel to the c-axis results in the release of one electron per vanadium ion; this leads to an abrupt jump in conductivity and the relaxation of the lattice to a tetragonal (rutile) structure [4–6].

These simultaneous electronic and first-order structural phase transitions (SPTs) have long been a hot topic of scientific debate, and competing theories attribute these changes to the Peierls lattice instability (a critical phonon density) and/or a critical carrier-density-dependent Mott transition [6, 7]. In addition to these pure aspects of VO$_2$ research, applied research indicates great potential in devices such as memristors, switches and sensors [8–12]. In switching and sensing applications, electric field-induced transitions (EFITs) offer a convenient method for instigating insulator to metal transitions (IMTs) [8–13]. Although EFITs have been widely studied in
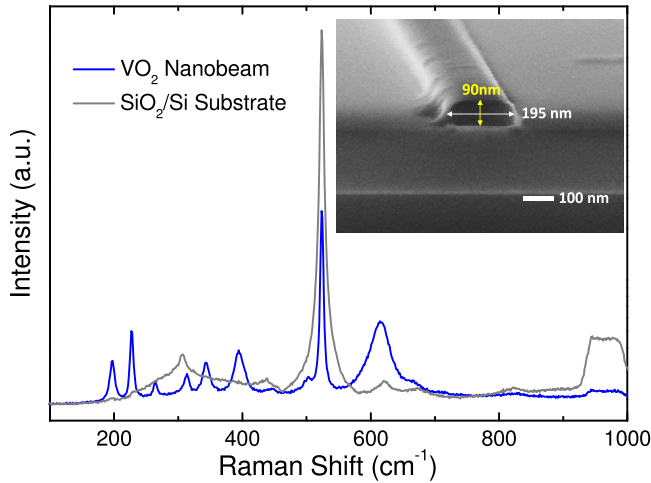
Figure 1. Raman spectrum of a monoclinic VO_2 NB alongside the background substrate signal. The inset shows a scanning electron microscope image of a VO_2 NB synthesized on a SiO_2–Si substrate at approximately 700 °C. The beam, observed end on, has a roughly rectangular cross-section.

the literature, their origin is under debate; both Joule heating and electric field effects have been proposed as the main factors behind the transition [14–24]. Recently, Zimmers *et al* [16] have proposed Joule heating as the main criteria in voltage based switching in VO_2 thin films.

However, conduction in VO_2 thin film after an EFIT becomes limited to a fraction of the whole channel, unlike in thermal heating induced transitions, where the whole channel is transformed from insulator to metal. This limitation can be overcome in VO_2 nanobeams (NBs), where the existence and propagation of single domains results in the transformation of the entire volume, both in the case of EFITs and thermally induced transitions. Moreover, VO_2 NBs are structurally and chemically uniform, and mechanically durable as compared to thin films, which share non-uniform stoichiometry, grain boundaries, residual stresses, etc, across the film/substrate interface [24–27]. Therefore, VO_2 NBs serve as a better model system for exploring the roles of electric field and Joule heating effects in first-order phase transitions in strongly correlated oxides.

The confirmation of the exact mechanisms involved in the EFITs in VO_2 NBs is the topic of this study. The experimental results were compared and correlated with both a simple power model and simulated results. Both the mathematical and simulated results match the experimental trends which validates the analysis.

2. Experiment methods

The VO_2 NBs were grown from a VO_2 powder source (Sigma-Aldrich Co.) using the vapour transport technique as described in previous work [13, 28]. Figure 1 shows the characteristic Raman spectrum of a representative VO_2 NB and the background substrate signal recorded at room temperature. The peaks in the Raman spectra of the VO_2 NB are identified at $197(A_g)$, $227(A_g)$, $264(B_g)$, $311(B_g)$,

$343(B_g)$, $396(A_g)$, $443(B_g)$, $614(A_g)$ cm^{-1}. The low-frequency phonons ($197(A_g)$ and $227(A_g)$) correspond to V–V lattice motion, and other distinguishable peaks relate to V–O bonding [28]. These Raman-active modes are the clear signature of the monoclinic (M1) phase predicted by its space group C_{2h}^5 and the measured M1 Raman spectra was also found to be consistent with previously reported measurements on VO_2 NBs [13, 18]. The NBs have rectangular cross-sections, as illustrated in the inset of figure 1, and a good aspect ratio of approximately 1 : 2. For the fabrication of NB devices, such as the one shown in figure 2, the grown VO_2 NBs were first detached from the SiO_2 substrate in iso-propyl alcohol (IPA) and then dispersed onto another clean substrate of 300 nm thick SiO_2 over p-type Si. Besides being helpful in selecting longer nanowires, this process reduces the substrate interaction effects with the VO_2 NBs in the transition measurements [28]. The selected NBs, as seen from an optical microscope, were contacted using UV photolithography where the desired electrode patterns were exposed to UV through the mask, and the resulting photoresist pattern was obtained after the developing process. Thereafter, an e-beam deposition of Ti/Au (10/150 nm) electrodes was carried out and finally a lift-off in acetone (to remove the photoresist layer) results in the pattern seen in figure 2. Further, rapid thermal annealing at 200 °C for 1 min was carried out in an argon environment at a flow rate of 1000 sccm and a pressure of 3.62 Torr for good ohmic contacts.

3. Results and discussion

Figure 3 shows the results of *I–V* measurements performed on a representative NB at room temperature; it indicates good ohmic contact formation with the Ti/Au (10/150 nm) electrodes. About 25 devices were fabricated for this experiment, and the resistance of each VO_2 NB varies from device to device. This is because VO_2 NBs have different dimensions and carrier densities (the latter are the result of fluctuations in the density of random defects, interstitials and vacancies formed during the growth process and cannot be precisely controlled). In order to eliminate any large variations, only those devices with similar dimensions were considered in this study. In spite of the small variations in individual characteristics, almost all the devices exhibited similar behaviours for all electric field and thermal studies. Figure 4 displays *I–V* curves recorded at different temperatures in the range of 296 to 365 K, and the inset illustrates the $\ln(R)$ versus $1/k_BT$ plot used to extract the activation energy (E_a) from the Arrhenius equation. The obtained value of 0.23 eV falls within the expected and reported range in the literature [4, 5].

Figure 5 shows a typical voltage hysteresis curve, measured at 55 °C so as to reduce the transition voltage, as measurements at room-temperature result in frequent breakdown of the devices due to the higher transition voltage. Furthermore, an upper current compliance of 1.0 mA was set in a Keithley 4200 SCS measurement system in order to avoid thermal burn-out of the NBs resulting from the excessive current flow after the transition. The transitions for upward and downward voltage sweeps (marked by diamonds) occurred
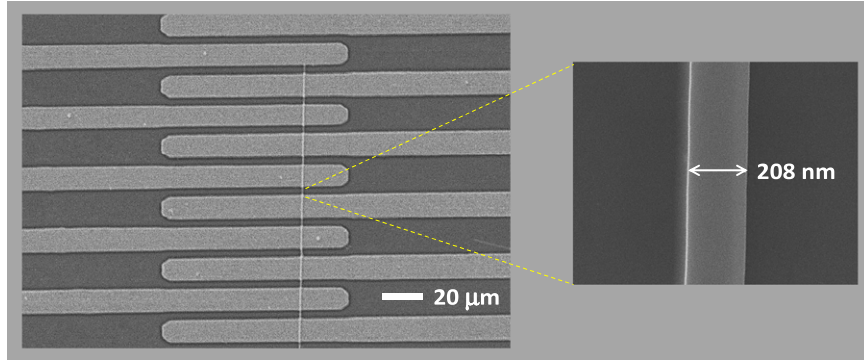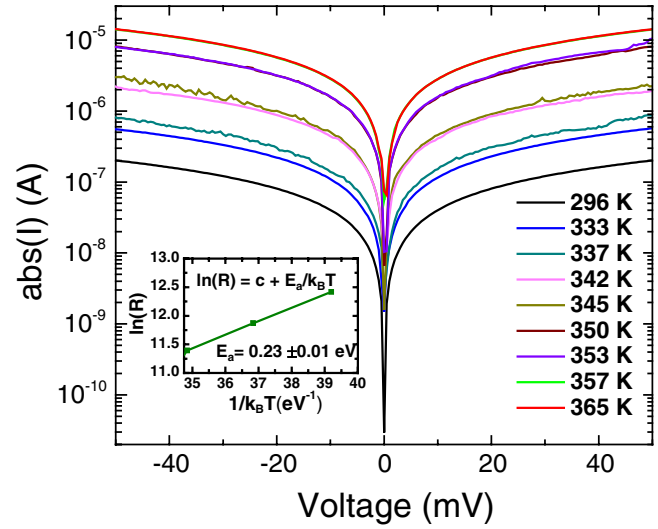
Figure 2. Scanning electron microscope image of the chip carrying the VO$_2$ NBs, and a higher magnification image of an individual NB with a width of 208 nm.
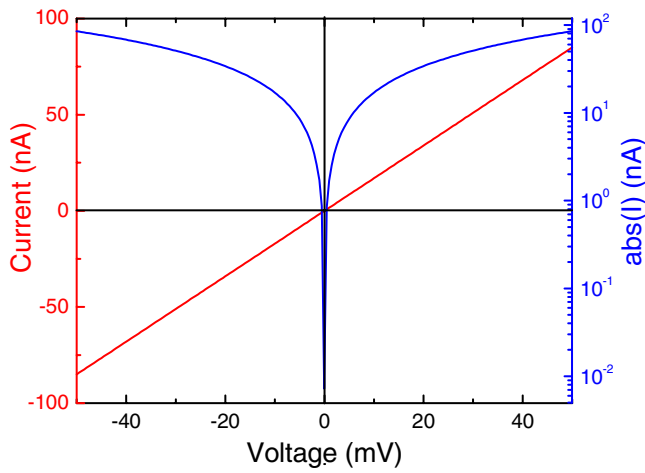
Figure 3. *I–V* characteristics of a VO$_2$ NB device at room temperature, with the red plots in a linear scale whereas the blue curve plots are in a semi-log scale.

Figure 4. The evolution of VO$_2$ NB *I–V* characteristics with temperature. The inset depicts the procedure for calculating the activation energy (E_a) from the thermally activated behaviour of the curves.

at around 3.2 V and 1.0 V, respectively. The inset shows the hysteretic temperature-triggered transition of the same device. As seen in the inset, the transition occurred at around 80 °C and 70 °C during heating and cooling, respectively.

A common feature observed in both the voltage- and temperature-induced transitions is the hysteresis window, which is a characteristic feature of the first-order phase transitions in VO$_2$ NBs and thin film devices. As a spontaneous, homogeneous, phase transition encompassing the whole NB would require a huge amount of energy, and hence remains thermodynamically unfeasible, so the phase change in VO$_2$ NBs propagates in a heterogeneous fashion via domain nucleation at defect sites where the free-energy barrier is low enough for the new phase to nucleate inside the parent phase [29–32]. Such phase transformations in NBs, occurring via nucleation and expansion of individual domains, have been widely reported [4, 33]. Moreover, the existence of an energy difference between the monoclinic and tetragonal domains requires additional coercive energy for complete transformation. This results in substantial overheating and undercooling (excess driving force) for the transformation from monoclinic to tetragonal phase and back, thereby all types of transition curves induced via the application of a voltage [8], heat [4], or a gate-field [3] exhibit hysteresis.

Moreover, studies indicate that the sharpness, shape, width and position of the hysteresis curve depend critically on the crystallinity, stoichiometry, distribution and activation of interstitial impurity/defect densities, and interface stresses in VO$_2$ with an underlying substrate [25, 31].

Figure 6 displays the dual-sweep *I–V* behaviour of a device, from −4.0 to +4.0 V and back, measured at 55 °C (with the schematic shown in figure 7(*a*)). Besides schematizing the orientation of vanadium atoms in the different phases, the inset images in figure 6 illustrate the VO$_2$ energy band diagrams based on the molecular orbital and crystal field theory employed by Goodenough [34], in which the d_{ll} band splits as the VO$_2$ undergoes a transition [1, 2]. Of the five transitions (four marked by diamonds and one by a star) in figure 6, the four diamond-marked transitions occurred during the course of the gradual voltage sweep, but the star-marked transition occurred upon the discontinuous/abrupt rise in voltage from no signal to −4.0 V. Such transitions, reported in the literature, are attributed to either electric field—and/or Joule heating—induced transitions, and it is debated whether the diamond transitions have both electric field and Joule heating origins or

J. Phys. D: Appl. Phys. **47** (2014) 295101

S Rathi *et al*
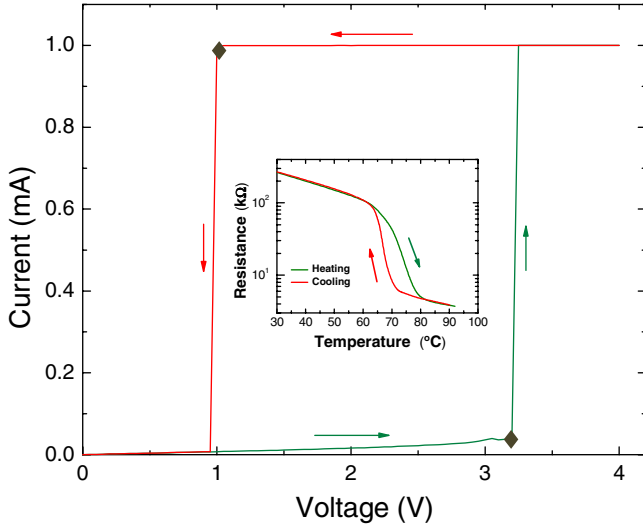
Figure 5. *I*–*V* curve indicating metal–insulator transitions in a VO$_2$ NB with an applied voltage measured at 55 °C. The inset shows thermally induced transition for both heating and cooling conditions.
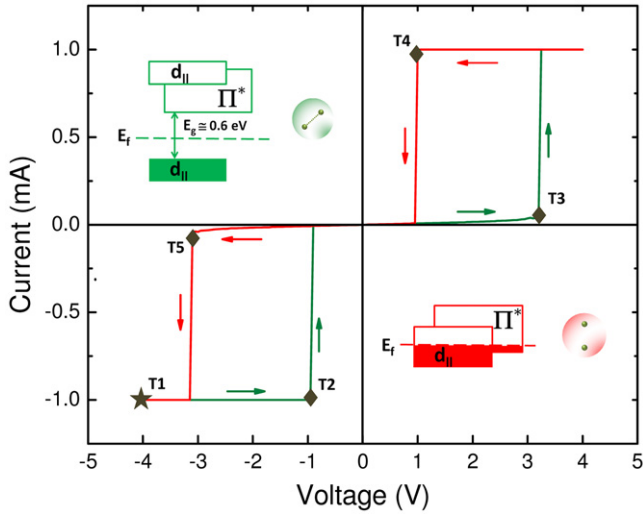
Figure 6. Dual-sweep *I*–*V* curve, measured at 55 °C, from negative to positive voltage. The star symbol (at T1) indicates the abrupt/instantaneous transition with the application of the signal. The diamond symbols (at T2, T3, T4, T5) represent transitions for increasing and decreasing voltage. The schematics in the inset illustrate the energy band diagram and vanadium atoms orientation in the insulating (green) and metallic (red) states.

result from Joule heating exclusively [16, 19, 35, 36]. We have studied these transitions, and our analysis indicates that Joule heating alone can produce the diamond transitions, while the star transition was initiated by the electric field-induced Poole–Frenkel (PF) effect, subsequently supported by Joule heating. We would describe the Joule heating transitions first and then analyse the PF transition behaviour.

3.1. Joule heating induced transitions

A simple power dissipation model is employed to examine Joule heating in a NB, which is counterbalanced by conductive losses to the atmosphere, metal electrodes, and the substrate.

In this model, the power dissipation can be expressed as [13]

$$dQ/dt = V_c^2/R_c - k(T - T_0),\tag{1}$$

where k is a collection of thermal parameters, including the thermal coefficient and heat capacity of the NB and the underlying substrate surface, V_c and R_c are the voltage and resistance across the NB, respectively, and T and T_0 are the temperature of NB and ambient environment, respectively. At equilibrium and for negligible ohmic contact resistance, equation (1) can be rearranged as

$$V_T = [k(T_T - T_0)R_A]^{1/2},\tag{2}$$

where R_A is the NB resistance before the transition, and V_T and T_T are the transition voltage and temperature, respectively. An analogous expression for V_T', the voltage at which the reverse transition occurs when voltage is swept from high to low, can also be deduced. This is

$$V_T' = [k'(T_T' - T_0)R_B]^{1/2},\tag{3}$$

where k' is the collection of thermal coefficients in the metallic phase at high temperature and R_B is the NB resistance in the metallic (rutile) phase.

Using equations (2) and (3), along with the derived constants k and k', V_T and V_T' were found to be in agreement with the observed values (in figure 6, the diamond symbols at T3 and T5, and T2 and T4 indicate V_T and V_T', respectively). To further confirm the nature of the transitions, the conductance and resistance below the transition point, i.e. for $V < 3.2$ V, are plotted in figure 7(*b*). From the figure, it can be observed that the variation is small at low V and increases rapidly after 2.0 V, until it results in a steep variation in the conductance near the transition point. Furthermore, if we compare the resistance variation trend in figure 7(*b*) to that of the inset in figure 5, they appear to be similar. To make this comparison between the two variations more clear, we solve equation (1) by assuming an instantaneous equilibrium with the environment, i.e.

$$T = T_0 + V^2/kR\tag{4a}$$

or

$$T = T_0 + IV/k.\tag{4b}$$

The above expressions are similar to the one used by Zimmers *et al* [16], which was fitted to the observed local temperature evolution in the VO$_2$ thin film channel. Using equations (4*a*) and (4*b*) and taking k as 4.6×10^{-6} W K^{-1}, we plot both thermal resistance and Joule heating induced resistance variation in figure 7(*c*). The excellent agreement of the two curves confirms that the voltage-induced transition in the VO$_2$ NBs is thermal in nature. On the other hand, according to Mott's theory, the transition occurs at a critical density of electrons, n_c, which is related to the screening due to electron–electron interactions and is given by [19, 20]

$$(n_c)^{1/3}\alpha_H \cong 0.25,\tag{5}$$

where $\alpha_H (= (\varepsilon_0\varepsilon_r/m^*)(\hbar/e)^2$ (where m^* is the electron effective mass, $\varepsilon_0\varepsilon_r$ is the permittivity of VO$_2$, and e is the
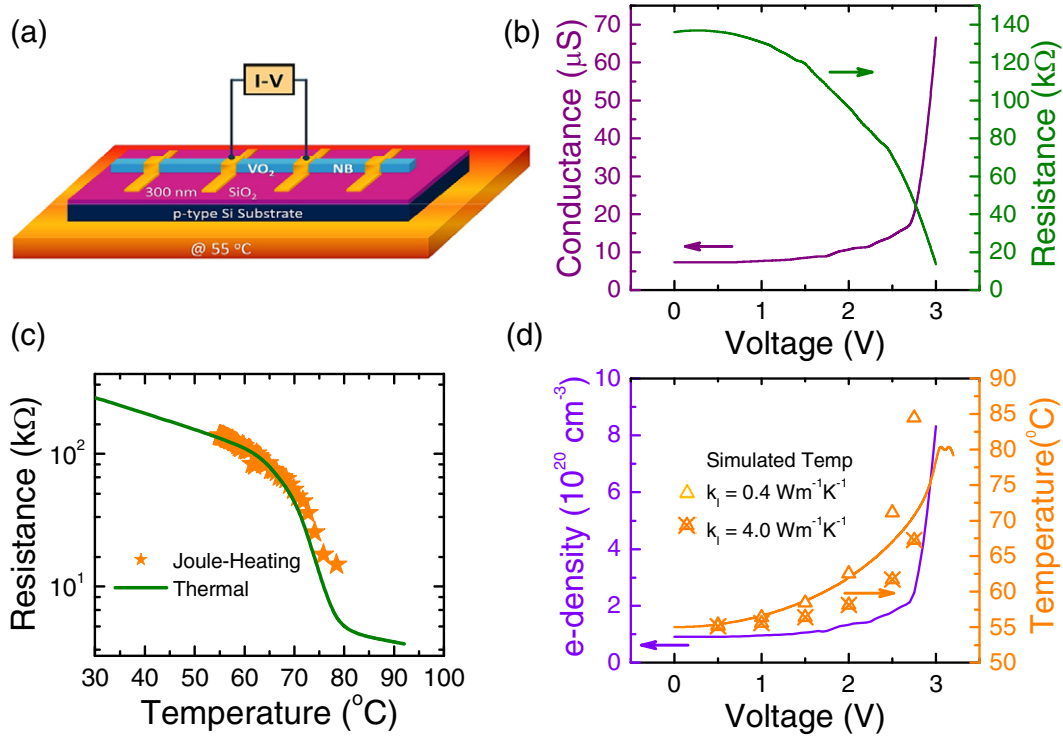
Figure 7. (*a*) Schematic of the measurement setup, carried out at 55 °C with the Keithley measurement unit. (*b*) Variation in conductance and resistance with applied voltage below the transition point ($V < V_T = 3.2$ V). (*c*) Thermal transition behaviour superimposed on that estimated for Joule heating using equations (4*a*) and (4*b*). (*d*) Variation in electron density and temperature with the applied voltage $V < V_T$, obtained from equations (4*a*) and (4*b*). The open and cross triangular symbols indicate the simulated temperature for two different thermal conductivities i.e. 0.4 and 4.0 W m^{-1} K^{-1}.

electron charge) is the localization radius of electrons in the insulating phase known as the Bohr radius. The critical density of electrons, n_c, is calculated as $\approx 10^{21}$ cm^{-3}, using ε_r and m^* as 28 and $7m_e$, respectively [37, 38, 43]. The electron density in the insulating state is also calculated from the measured conductivity by considering the carrier mobility as 0.5 cm^2 V^{-1} s^{-1} which is within the range of reported values i.e. 0.1–1.0 cm^2 V^{-1} s^{-1} [37, 38]. It can be seen from figure 7(*d*) that, as the transition point is approached, the Joule heating induced temperature rises steeply along with the electron density in the voltage-induced transition.

To further validate this thermal behaviour, a finite element method (FEM) simulation was carried out [39]. Various models for Joule heating, heat transfer, convective cooling, and heat loss via radiations have been incorporated for a realistic simulation, along with the relevant material parameters. The variation in the conductivity at different voltages is also considered in the simulations. Other VO$_2$ material parameters considered in the simulations are specific heat, $C = 690$ J kg^{-1} K^{-1}, mass density, $\rho = 4340$ kg m^{-3}, relative permittivity, $\varepsilon_r = 24$, Young's Modulus, $E = 120 \times 10^9$ Pa, thermal conductivity, $k_1 = 0.4$ W m^{-1} K^{-1}, Poisson's ratio = 0.2, and coefficient of thermal expansion, $\alpha = 23.2 \times 10^{-6}$ K^{-1}. These values have been widely reported [2, 3, 6, 13, 19] for VO$_2$ except the considered thermal conductivity. The thermal conductivity for VO$_2$ thin films [40] has been reported as ≈ 4 W m^{-1} K^{-1} but in the absence of any reported values for VO$_2$ NBs in the literature, we found 0.4 W m^{-1} K^{-1} matches well with our experimental results as illustrated in figure 7(*d*). Similar reductions in thermal

conductivity from bulk to nanowire have been widely reported for other nanowires [41, 42] like silicon, InAs, etc, where this has been mainly attributed to the higher phonon boundary scattering on the nanowire surface due to the higher surface to volume ratio in low-dimensional materials. Figures 8(*a*)–(*c*) illustrate the device geometry considered for the simulation, and a representative case when a voltage of 2 V is applied across the NB along with the zoom-in detail of the metal-NB region. It can be seen that the temperature across the NB is at a maximum in the middle, while it falls near the electrode due to the better thermal conductivity of metal electrodes which work as effective heat sinks.

The matching of the simulated results with the modelled one is another indication of the accuracy of the model employed for Joule heating, although the simulated values show considerable differences as the transition point is approached. This can possibly be the result of the static values of the material properties used in the simulation, as the material properties such as thermal conductivity, lattice constant, etc, start varying near the transition point [39].

3.2. PF effect induced transition

Using this elaboration on the gradual transitions, marked by diamonds (figure 6), we can now focus on the first transition, marked by the star in figure 6. For clarity, figure 9 re-plots the data used in figure 6 in the time domain, where it can be seen that the first transition occurs almost instantaneously with the applied voltage. Further, both absolute current and voltage are plotted in figure 9 on the common time

J. Phys. D: Appl. Phys. **47** (2014) 295101

S Rathi *et al*
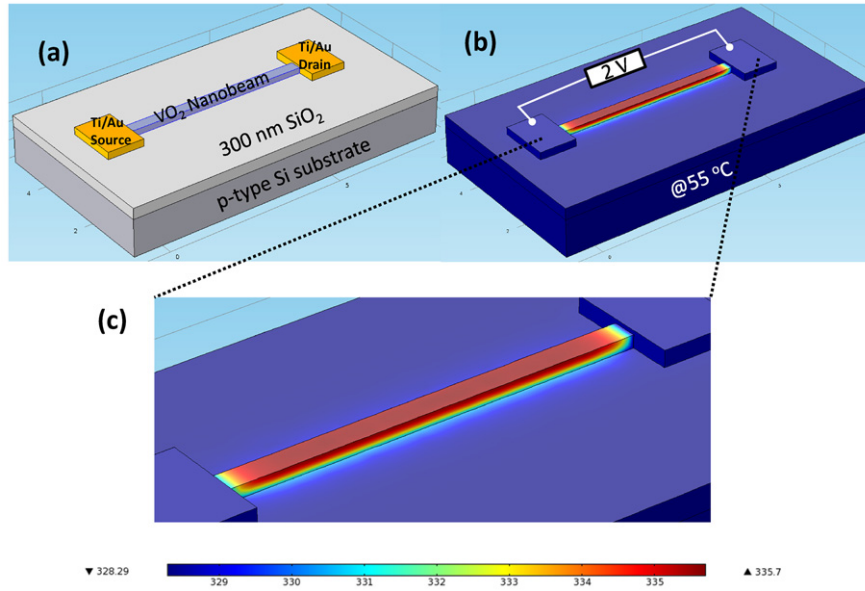
Figure 8. FEM simulated temperature variation in VO$_2$ NB on the SiO$_2$/ p-Si substrate. (*a*) Schematic of the simulated device. (*b*) Temperature variation in the device due to an applied voltage of 2 V. (*c*) Zoom-in details of the temperature variations near the metal pads and oxide interface, with the colour scale at the bottom.

scale for a clearer perspective, and the top plot illustrates the variation in current in the logarithmic scale as the NB undergoes repeated transitions. The first abrupt transition can be explained in terms of the PF effect, which could lead to a sudden jump in the conductivity and, subsequently, an abrupt increase in the temperature due to Joule heating, resulting in the transition. FEM simulations show that the conductivity of 500–700 S m^{-1} at 55 °C is not enough to reach the transition temperature instantaneously under a direct applied electric field $\cong$ 10 kV cm^{-1} (4 V in 5 μm electrode gap). However, by considering the PF effect, the initial conductivity is enhanced by approximately an order of magnitude, which results in a higher temperature due to Joule heating, thus reaching the transition temperature. This PF-induced conductivity enhancement is illustrated in the inset of figure 10, where a sudden increase in voltage across the NBs results in the lowering of the Coulomb-induced activation barrier by $\beta\sqrt{E(t)}$, where $E(t)$ is the time-varying electric field and β is the PF constant. This leads to a higher carrier concentration and hence higher conductivity in the NB [37, 43]. Mathematically, it can be expressed as

$$\sigma(t) = \sigma_0 \exp\left[\beta\sqrt{E(t)}/rk_{\rm B}T\right], \qquad (6)$$

where $\sigma(t)$ is the conductivity at time t, σ_0 is initial conductivity, T is the temperature, $\beta = 2\left(e^3/\varepsilon_0\varepsilon_{\rm r}\right)^{1/2}$ is the PF constant, and r is the PF slope parameter, whose value varies from 1 to 2, depending upon the position of the Fermi level [37, 43]. The abrupt electric field induced increase in the carrier concentration (and conductivity) subsequently leads to carrier acceleration under the applied electric field, which results in Joule heating, and thus a rise in temperature. This physical process can be modelled by the two temperature coupled equations [37], given by

$$C_{\rm e}{\rm d}T_{\rm e}/{\rm d}t = -G\left(T_{\rm e} - T_{\rm i}\right) + \sigma(t)\left[E(t)\right]^2 \qquad (7a)$$

and

$$C_{\rm i}{\rm d}T_{\rm i}/{\rm d}t = G\left(T_{\rm e} - T_{\rm i}\right), \qquad (7b)$$

where $\{T_{\rm e}, C_{\rm e}\}$ and $\{T_{\rm i}, C_{\rm i}\}$ are the electron and lattice {temperature, specific heat}, respectively, and G is the electron–phonon coupling coefficient for VO$_2$. In equations (7*a*) and (7*b*), the Joule heating induced abrupt rise (given by the second term in equation (7*a*)) in electron temperature leads to an increase and subsequent stabilization of the lattice temperature.

The two temperature coupled equations have been solved using numerical methods with the values of electron specific heat coefficient, $\gamma = 1.4 \times 10^{-2}$ J mol^{-1} K^{-2} and electron–phonon coupling coefficient $G = 10^{18}$ W K^{-1} m^{-3}. It can be seen from figure 10 that an abrupt rise in the electron temperature occurs when an electric field is applied at an arbitrary point in time. These highly energetic electrons rapidly heat up the lattice via electron–phonon interactions, resulting in an increase in lattice temperature [37]. This energy relaxation from electron to lattice can occur in the order of picoseconds, and the increase in lattice temperature is of the same order as that required for the metal–insulator transition in VO$_2$ NBs. Although the exact dynamics involved in the transition process are more complicated than pictured above (because of concerns related to resistive-capacitive (RC) delay, the energy required for SPTs, etc), but the increase in temperature is in the range of the transition temperature, so therefore the PF effect satisfactorily explained the observed instantaneous transition in figures 6 and 9 (marked by the star symbols).

From figure 10, it appears that the transition should occur in the picosecond scale, whereas the data recording capabilities of the Keithley measurement system cannot capture transitions below the decisecond scale. Also, the minimum switching time ($t_{\rm min}$) for such electric field induced switching, observed via
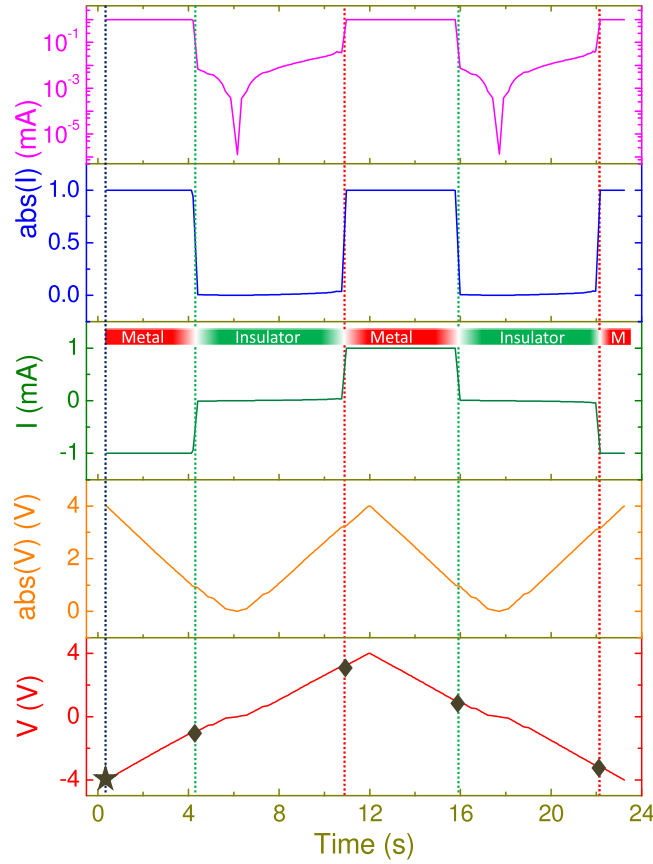
Figure 9. Time evolution plot of the $I-V$ data in figure 6. The red curve indicates voltage, the orange curve indicates the absolute voltage, the green curve shows current variation, and the blue curve shows the absolute current. The pink curve shows the current variation in a semi-log scale.

$I-V$ measurement, can be calculated [19, 35] by considering the thermal parameters of VO$_2$ NBs only for the constant k in equation (2) as

$$t_{min} = (C\rho V_{ch})(T_T - T_0)R/V^2, \qquad (8)$$

where C is specific heat, ρ is mass density, and V_{ch} is the NB channel volume. Considering a NB of dimension $V_{ch} =$ length $\times$ width $\times$ height $= 5\,\mu m \times 300\,nm \times 150\,nm$, with a given resistance R, under an applied voltage V, near the transition point, t_{min} is in the order of 10 nanoseconds (ns). This timescale is further confirmed by the comparison of the value of the term $C\rho V_{ch}/t_{min}$ with that of the experimentally obtained k. Therefore, in order to resolve the observed transition time further, an oscilloscope measurement with a square pulse of $1\,\mu s$ duration was carried out, and it can be seen in the inset of figure 11 that the transition time is in the order of 100 ns. An initial delay in onset time can still be seen in the oscilloscope measurement; this may be due to the intrinsic RC factor associated with the NB and the external resistance and hence is difficult to remove completely [23, 24, 44]. However, this RC delay can be overcome using ultrafast time-resolved THz spectroscopy/pump–probe techniques, where the transitions time in the VO$_2$ material is in the order of the picosecond scale [6, 37]. Further, Treadway *et al* [24] have demonstrated that
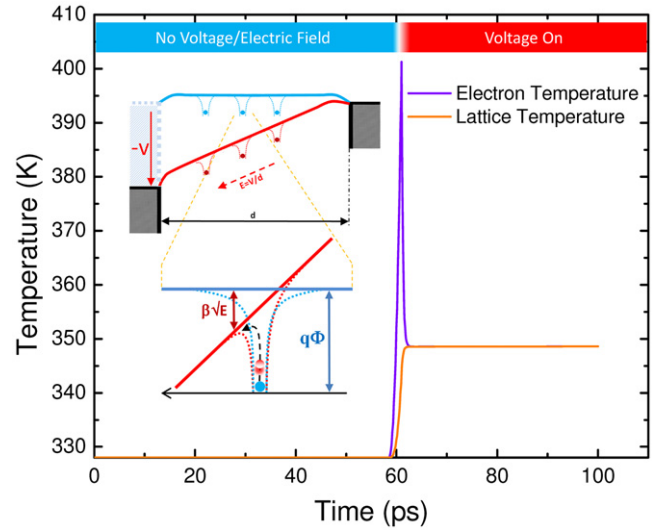
Figure 10. Illustration of electron and lattice temperature variations with the application of a high-voltage signal at $t \approx 58$ ps. The schematic in the inset illustrates the lowering of barrier height on the application of the abrupt voltage signal, and the symbols q, Φ and d represent fundamental charge, initial barrier for no field, and distance between two consecutive electrodes, respectively.
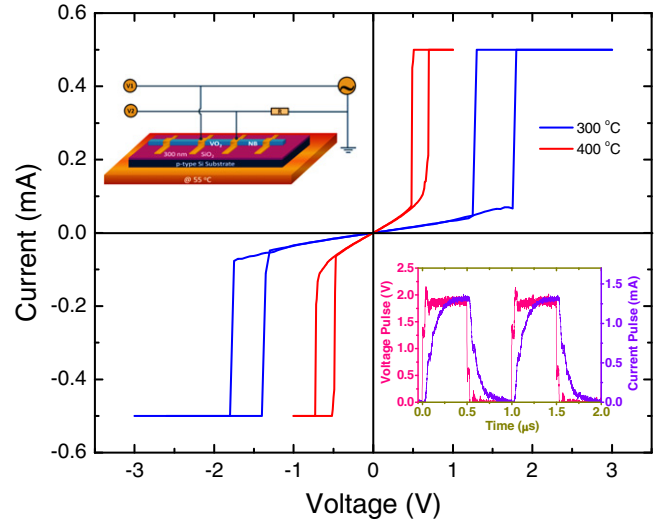
Figure 11. $I-V$ curve measured at 55 °C for VO$_2$ NBs annealed at 300 and 400 °C in an argon ambient for 1 min. The top left inset illustrates the arrangement for the oscilloscope measurement, plotted in the bottom right inset. A square input pulse was applied to the device annealed at 300 °C, and the voltage drop was recorded using an oscilloscope across an external resistance, which was then converted and plotted as current.

radio frequency (RF) power also contributes to the dc voltage-induced switching in the VO$_2$ thin-film-based coplanar waveguides, and the RF based steady-state switching time is of the same order as t_{min}. This also indicates toward the two process-based mechanism where field-induced carrier injection results in an initial current jump, followed by the temperature rise due to Joule heating [24].

Furthermore, the $I-V$ curves in figure 11 show the transition characteristics of NBs annealed at 300 and 400 °C in an argon ambient for 1 min. It can be seen from the figure that the annealing results in the lowering of the transition voltage for both abrupt and gradual transitions.

This fits the Joule heating and PF effect based transition pictures as annealing in the reducing environment decreases the NB's resistance from $500\,k\Omega$ (standard device annealed at $200\,°C$) to $250\,k\Omega$ and $42\,k\Omega$ for devices annealed at $300\,°C$ and $400\,°C$, respectively, which results in reduced threshold voltages to achieve the transition. The decrease in NB resistance is due to oxygen deficiency induced lattice defects, like interstitials and vacancies, along with the formation of various Magnéli phases ($V_nO_{2n-1} = V_2O_3 + (n-2)\,VO_2$) which result in higher electron concentrations [28, 45, 46]. Moreover, according to the Drude model of conductivity ($\sigma = ne\mu$, where n is carrier concentration, e is charge and μ is mobility), the decrease in the NB's resistance also indicates higher electron concentrations, as annealing induced imperfections and defects in the crystal lattice would result in mobility degradation rather than enhancement. The lowering of the transition voltage in figure 11 is also consistent with Mott's transition theory, in which the transition is dependent on the critical strength of electron-density dependent screening.

4. Conclusion

In conclusion, both abrupt and gradual transitions have been observed in VO_2 nanobeam devices upon the application of a dual-sweep voltage signal. The gradual transitions agree with the Joule heating picture, while the Poole–Frenkel effect fits for the abrupt transition. Although an intrinsic RC delay limits the abrupt transition time in electrical switching, it can still be utilized for switching and fail-safe applications. Furthermore, this study can also serve as a comprehensive guide for understanding the electrical response of vanadium dioxide nanobeams for device applications.

Acknowledgments

References

[1] Imada M, Fujimori A and Tokura Y 1998 *Rev. Mod. Phys.* **70** 4
[2] Yang Z, Ko C and Ramanathan S 2011 *Annu. Rev. Mater. Res.* **41** 337
[3] Nakano M, Shibuya K, Okuyama D, Hatano T, Ono S, Kawasaki M, Iwasa Y and Tokura Y 2012 *Nature* **487** 459
[4] Wei J, Wang Z, Chen W and Cobden D H 2009 *Nature Nanotechnol.* **4** 420
[5] Wei J, Ji H, Guo W, Nevidomskyy A H and Natelson D 2012 *Nature Nanotechnol.* **7** 357
[6] Cocker T L, Titova L V, Fourmaux S, Holloway G, Bandulet H C, Brassard D, Kieffer J C, Khakani M A E and Hegmann F A 2012 *Phys. Rev. B* **85** 155120
[7] Eyert V 2011 *Phys. Rev. Lett.* **107** 016401
[8] Baik J M, Kim M H, Larson C, Yavuz C T, Stucky G D, Wodtke A M and Moskovits M 2009 *Nano Lett.* **9** 3980
[9] Strelcov E, Lilach Y and Kolmakov A 2009 *Nano Lett.* **9** 2322
[10] Sengupta S, Wang K, Liu K, Bhat A K, Dhara S, Wu J and Deshmukh M M 2011 *Appl. Phys. Lett.* **99** 062114
[11] Pellegrino L, Manca N, Kanki T, Tanaka H, Biasotti M, Bellingeri E, Siri A S and Marré D 2012 *Adv. Mater.* **24** 2929
[12] Manca N, Pellegrino L, Kanki T, Yamasaki S, Tanaka H, Siri A S and Marré D 2013 *Adv. Mater.* **25** 6430
[13] Baik J M, Kim M H, Larson C, Wodtke A M and Moskovits M 2008 *J. Phys. Chem. C* **112** 13328
[14] Yang Z, Hart S, Ko C, Yacoby A and Ramanathan S 2011 *J. Appl. Phys.* **110** 033725
[15] Fu D, Liu K, Tao T, Lo K, Cheng C, Liu B, Zhang R, Bechtel H A and Wu J 2013 *J. Appl. Phys.* **113** 043707
[16] Zimmers A, Aigouy L, Mortier M, Sharoni A, Wang S, West K G, Ramirez J G and Schuller I K 2013 *Phys. Rev. Lett.* **110** 056601
[17] Ko C and Ramanathan S 2008 *Appl. Phys. Lett.* **93** 252101
[18] Kim H T, Chae B G, Youn D H, Kim G, Kang K Y, Lee S J, Kim K and Lim Y S 2005 *Appl. Phys. Lett.* **86** 242101
[19] Stefanovich G, Pergament A and Stefanovich D 2000 *J. Phys.: Condens. Matter* **12** 8837
[20] Hormoz S and Ramanathan S 2010 *Solid-State Electron.* **54** 654
[21] Lee S B, Kim K, Oh J S, Kahng B and Lee J S 2013 *Appl. Phys. Lett.* **102** 063501
[22] Zhou Y, Chen X, Ko C, Yang Z, Mouli C and Ramanathan S 2013 *IEEE Electron Device Lett.* **34** 2
[23] Kar A, Shukla N, Freeman E, Paik H, Liu H, Herbert R E, Bharadwaja S S N, Schlom D G and Datta S 2013 *Appl. Phys. Lett.* **102** 072106
[24] Ha S D, Zhou Y, Fisher C J, Ramanathan S and Treadway J P 2013 *J. Appl. Phys.* **113** 184501
[25] Yang Z, Ko C and Ramanathan S 2010 *J. Appl. Phys.* **108** 073708
[26] Ruzmetov D, Senanayake S D and Ramanathan S 2007 *Phys. Rev. B* **75** 195102
[27] Ruzmetov D, Senanayake S D, Narayanamurti V and Ramanathan S 2008 *Phys. Rev. B* **77** 195442
[28] Rathi S, Park J H, Lee I Y, Kim M J, Baik J M and Kim G H 2013 *Appl. Phys. Lett.* **103** 203114
[29] Atkin J M, Berweger S, Chavez E K, Raschke M B, Cao J, Fan W and Wu J 2012 *Phys. Rev. B* **85** 020101
[30] Lopez R, Haynes T E, Boatner L A, Feldman L C and Haglund R F 2002 *Phys. Rev. B* **65** 224113
[31] Donev E U, Lopez R, Feldman L C and Haglund R F 2009 *Nano Lett.* **9** 702
[32] Appavoo K, Lei D Y, Sonnefraud Y, Wang B, Pantelides S T, Maier S A and Haglund R F 2012 *Nano Lett.* **12** 780
[33] Sohn J I, Joo H J, Ahn D, Lee H H, Porter A E, Kim K, Kang D J and Welland M E 2009 *Nano Lett.* **9** 3392
[34] Goodenough J B 1971 *J. Solid State Chem.* **3** 490
[35] Gopalakrishnan G, Ruzmetov D and Ramanathan S 2009 *J. Mater. Sci.* **44** 5345
[36] Zhao Y, Hao J, Chen C and Fan Z 2012 *J. Phys.: Condens. Matter* **24** 035601
[37] Liu M et al 2012 *Nature* **487** 345
[38] Yang Z, Ko C, Balakrishnan V, Gopalakrishnan G and Ramanathan S 2010 *Phys. Rev. B* **82** 205101
[39] COMSOL Multiphysics Package (www.comsol.com/)
[40] Oh D W, Ko C, Ramanathan S and Cahill D G 2010 *Appl. Phys. Lett.* **96** 151906
[41] Li D, Wu Y, Kim P, Shi L, Yang P and Majumdar A 2003 *Appl. Phys. Lett.* **83** 14
[42] He Y and Galli G 2012 *Phys. Rev. Lett.* **108** 215901
[43] Hormoz S and Ramanathan S 2010 *Solid-State Electron.* **54** 654
[44] Zhou Y, Chen X, Ko C, Yang Z, Mouli C and Ramanathan S 2013 *IEEE Electron Device Lett.* **34** 220
[45] Zhang S, Kim I S and Lauhon L J 2011 *Nano Lett.* **11** 1443
[46] Hong W K et al 2013 *Nano Lett.* **13** 1822